

Four Cold Super-Jupiters Revealed by Extended and Complex Microlensing Signals

CHEONGHO HAN,¹ CHUNG-UK LEE,² MICHAEL D. ALBROW,³ SUN-JU CHUNG,² ANDREW GOULD,⁴ YOUN KIL JUNG,^{2,5} KYU-HA HWANG,² YOON-HYUN RYU,² YOSSI SHVARTZVALD,⁶ IN-GU SHIN,⁷ JENNIFER C. YEE,⁸ WEICHENG ZANG,⁷ HONGJING YANG,⁷ DOEON KIM,¹ DONG-JIN KIM,² SANG-MOK CHA,^{2,9} SEUNG-LEE KIM,² DONG-JOO LEE,² YONGSEOK LEE,^{2,9} BYEONG-GON PARK² AND RICHARD W. POGGE⁴

(KMTNET COLLABORATION)

¹Department of Physics, Chungbuk National University, Cheongju 28644, Republic of Korea

²Korea Astronomy and Space Science Institute, Daejon 34055, Republic of Korea

³University of Canterbury, Department of Physics and Astronomy, Private Bag 4800, Christchurch 8020, New Zealand

⁴Department of Astronomy, Ohio State University, 140 West 18th Ave., Columbus, OH 43210, USA

⁵University of Science and Technology, Daejeon 34113, Republic of Korea

⁶Department of Particle Physics and Astrophysics, Weizmann Institute of Science, Rehovot 76100, Israel

⁷Department of Astronomy, Westlake University, Hangzhou 310030, Zhejiang Province, China

⁸Center for Astrophysics | Harvard & Smithsonian 60 Garden St., Cambridge, MA 02138, USA

⁹School of Space Research, Kyung Hee University, Yongin, Gyeonggi 17104, Republic of Korea

ABSTRACT

We present the analysis of four microlensing events, KMT-2020-BLG-0202, KMT-2022-BLG-1551, KMT-2023-BLG-0466, and KMT-2025-BLG-0121, which exhibit extended and complex anomalies in their light curves. These events were identified through a systematic reanalysis of KMTNet data aimed at detecting planetary signals that deviate from the typical short-term anomaly morphology. Detailed modeling indicates that all four anomalies were produced by planetary companions to low-mass stellar hosts. The events have mass ratios of $q \sim (5-14) \times 10^{-3}$ and Einstein timescales of $t_E \sim 20-43$ days. Bayesian analyses based on Galactic models show that the companions are super-Jupiters with masses of a few to approximately $10 M_J$, orbiting sub-solar-mass hosts located at distances of $D_L \sim 4-7$ kpc. All planets lie well beyond the snow line of their hosts, placing them in the regime of cold giant planets. These detections demonstrate that extended and complex microlensing anomalies, which are often challenging to recognize as planetary in origin, can nonetheless contain planetary signals. This work underscores the unique sensitivity of microlensing to cold, massive planets beyond the snow line and highlights the importance of systematic reanalyses of survey data for achieving a more complete and unbiased census of exoplanets in the Galaxy.

Keywords: Gravitational microlensing exoplanet detection (2147)

1. INTRODUCTION

Planetary perturbations in gravitational microlensing events typically manifest as short-lived anomalies superimposed on an otherwise smooth and symmetric single-lens light curve. These deviations, which generally last from a few hours to a few days, arise when the source star passes near a small caustic induced by the planet-host system (S. Mao & B. Paczyński 1991; A. Gould & A. Loeb 1992). Because these signals exhibit distinctive features confined to a small region of

the light curve, they can be readily identified by high-cadence surveys and have served as the primary channel for microlensing planet discoveries to date.

However, planetary signals do not always conform to this typical morphology. Under certain lens configurations, planets can produce extended and complex anomalies that differ substantially from the typical short-duration perturbation. Such cases arise when the source trajectory interacts with both the central and planetary caustics or when the planet-host separation approaches the resonant regime, where two or three caustics merge into a single enlarged structure. Depending on the source trajectory, these resonant or near-resonant configurations can smooth, broaden, or

Corresponding author: cheongho@astroph.chungbuk.ac.kr

Corresponding author: leecu@kasi.re.kr

Table 1. Event coordinates, fields, observational cadence, and I -band extinction.

ID reference	(RA, DEC) _{J2000}	(l, b)	Field	Cadence	A_I
KMT-2020-BLG-0202	(17:48:09.71, -24:28:28.02)	($4^\circ.1100, 1^\circ.8282$)	BLG19	1.0 hour	2.82
KMT-2022-BLG-1551	(17:41:00.90, -27:33:06.77)	($0^\circ.6457, 1^\circ.5899$)	BLG15	1.0 hour	3.18
KMT-2023-BLG-0466	(18:02:26.40, -33:00:10.69)	($-1^\circ.6930, -5^\circ.1640$)	BLG34	2.5 hour	0.97
KMT-2025-BLG-0121	(17:48:38.01, -23:59:55.68)	($4^\circ.5733, 1^\circ.9812$)	BLG19	1.0 hour	2.09

elongate the magnification pattern, leading to anomalies with multiple substructures.

A major difficulty is that extended planetary perturbations can closely resemble anomalies produced by binary lenses that have comparable component masses. This similarity makes it difficult to distinguish planetary systems from equal-mass binaries based solely on light-curve shape. The problem is further compounded by the large number of binary-lens events in survey data, which imposes substantial practical and computational burdens when searching for the much smaller planetary subset. Consequently, achieving a complete census of planetary microlensing events requires systematic and detailed modeling of a large number of anomalous light curves.

To address this challenge, C. Han et al. (2021, hereafter Paper I) carried out a dedicated reanalysis of the 2017–2019 microlensing survey data, focusing on planetary events whose signatures were difficult to identify because they deviated from the standard short-term anomaly morphology. The analysis begins by identifying candidate anomalous events. Each light curve is fit with a 1L1S model, and both cumulative and localized residuals are examined to flag statistically significant and temporally coherent deviations. Events that meet these criteria are then prioritized for more sophisticated modeling, such as planetary, binary-lens, or binary-source interpretations. The overall modeling strategy is hierarchical and iterative, advancing from simple to increasingly complex descriptions until the observed anomalies are reproduced in a physically consistent manner. This effort uncovered three previously unrecognized planets—KMT-2017-BLG-2509Lb, OGLE-2017-BLG-1099Lb, and OGLE-2019-BLG-0299Lb—whose light curves displayed extended anomalies produced by source crossings of resonant caustics generated by giant planets located near the Einstein rings of their hosts. These discoveries demonstrated that planets exhibiting extended and complex anomaly patterns can be missed, underscoring the importance of systematic reexaminations of microlensing data to improve detection completeness.

Building on the approach of Paper I, we extended this effort to microlensing events detected from 2020 to 2025 with the goal of identifying additional planetary systems that exhibit extended or complex anomalies. Through analyses of anomalous lensing events detected from this period, we discovered four new planets: KMT-2020-BLG-0202Lb, KMT-2022-BLG-1551Lb, KMT-2023-BLG-0466Lb, and KMT-2025-BLG-0121Lb. In this paper, we present detailed analyses of these events and discuss their implications for understanding planetary systems that generate extended microlensing anomalies.

2. OBSERVATIONS AND DATA

The four lensing events were detected exclusively by the Korea Microlensing Telescope Network (KMTNet; S.-L. Kim et al. 2016) survey. The survey was established to conduct high-cadence, wide-field photometric monitoring of dense stellar fields toward the Galactic bulge, with the goal of discovering and characterizing gravitational microlensing events, including those produced by exoplanets.

KMTNet consists of three identical 1.6 m telescopes, each equipped with a 4 deg^2 field-of-view camera, located at the Cerro Tololo Inter-American Observatory in Chile (KMTC), the South African Astronomical Observatory in South Africa (KMTS), and the Siding Spring Observatory in Australia (KMTA). This global configuration enables continuous, round-the-clock monitoring of the Galactic bulge, allowing high-cadence observations throughout the bulge season. Most images are obtained in the I band, with roughly 10% V -band frames acquired for color information.

Table 1 lists the equatorial and Galactic coordinates of the analyzed events, along with the corresponding KMTNet fields, observation cadences, and I -band extinctions toward the respective fields. For KMT-2022-BLG-1551, supplementary data were acquired through follow-up observations conducted with the 1.0 m telescope of the Las Cumbres Observatory at the South African Astronomical Observatory site (LCOS). The follow-up images were acquired at two main epochs: near the peak of the event and during the declining

Table 2. Number of data points and error-bar readjustment factors.

Telescope	Data set	N_{data}	k	σ_{min}
KMT-2020-BLG-0202	KMTA19	441	0.843	0.010
KMT-2022-BLG-1551	KMTC15	945	1.217	0.020
	KMTS15	583	1.288	0.020
	KMTA15	295	1.513	0.010
	LCOS	32	0.949	0.004
KMT-2023-BLG-0466	KMTC34	493	0.648	0.010
	KMTS34	237	0.980	0.010
	KMTA34	266	0.794	0.010
KMT-2025-BLG-0121	KMTC19	1012	0.806	0.020
	KMTS19	438	0.787	0.020
	KMTA19	425	0.830	0.020

phase of the light curve. All follow-up observations were conducted in the I band.

Both the survey and follow-up data were reduced with the KMTNet photometric pipeline (M. D. Albrow et al. 2009), which is based on the difference-image-analysis (DIA) method (A. B. Tomaney & A. P. S. Croots 1996; R. H. Alard 1998; P. R. Wozniak 2000). This technique is particularly effective for crowded stellar fields toward the Galactic bulge, where blending is severe, and it yields high-precision relative photometry suitable for microlensing analyses. For optimal data fidelity, the KMTNet dataset was reprocessed with the new tender-love care photometry pipeline described in H. Yang et al. (2025). For each event, the photometry from the three KMTNet sites was processed independently and then combined to construct its light curve. During this process, the photometric uncertainties were empirically renormalized so that each data set satisfies $\chi^2/\text{dof} \simeq 1$ for the best-fit model. The renormalization followed the procedure described by J. C. Yee et al. (2012). In particular, the error bars were adjusted according to

$$\sigma' = k \sqrt{\sigma^2 + \sigma_{\text{min}}^2}, \quad (1)$$

where σ denotes the reported uncertainty, k is a multiplicative scale factor, and σ_{min} represents a systematic error floor. In Table 2, we list the error-bar renormalization factors and the number of data points (N_{data}) for each data set.

3. LIGHT CURVE ANALYSES

The light curves of all analyzed events show prominent caustic-related features, indicating that the lenses are multiple systems. Accordingly, we begin our analysis

by modeling the light curves with a binary-lens single-source (2L1S) framework.

The modeling of the light curve was carried out to determine a lensing solution, which represents a set of parameters describing the observed light curve. The light curve of a 2L1S event is characterized by seven basic parameters ($t_0, u_0, t_E, s, q, \alpha, \rho$). Three of these describe the lens-source geometry: t_0 is the time of the closest approach between the source and the reference position of the lens, u_0 is the impact parameter (the lens-source separation at t_0) in units of the angular Einstein radius θ_E , and t_E is the Einstein timescale, defined as the time required for the source to traverse θ_E . Two additional parameters characterize the binary nature of the lens: s denotes the projected separation between the lens components (M_1 and M_2) in units of θ_E , and q represents their mass ratio. The parameter α specifies the orientation of the source trajectory with respect to the binary-lens axis. Finally, the parameter ρ , defined as the ratio of the angular source radius to θ_E , accounts for finite-source effects that become important during caustic crossings or approaches.

We search for a lensing solution in two stages. We first perform a grid search over (s, q) , for which the magnification is highly sensitive to small parameter changes, while optimizing the remaining parameters via downhill minimization with initial guesses based on basic light-curve features such as event epoch, peak magnification, and timescale. For the source-trajectory angle α , we use 20 uniformly spaced trial values over 0 – 2π . The resulting χ^2 maps in the (s, q) plane are used to locate local minima (candidate solutions). We then refine each candidate by allowing all parameters to vary simultaneously. If multiple solutions remain, we assess degeneracies by comparing their χ^2 values. All modeling is carried out with a custom code based on the map-making method of S. Dong et al. (2006), using ray shooting to compute finite-source magnifications. In our modeling, we do not include higher-order effects because the event timescales are not long enough and the light curves show no clear signatures of such effects.

In the following subsections, we present detailed analyses of the individual events. For each event, we begin by briefly describing the data sets used and identifying the distinctive anomaly observed in the light curve. We then present the corresponding lensing model and best-fit solution, followed by a discussion of how the observed anomaly is explained within the binary-lens framework.

3.1. KMT-2020-BLG-0202

The lensing event KMT-2020-BLG-0202 was detected on 2020 April 17, which corresponds to the abridged He-

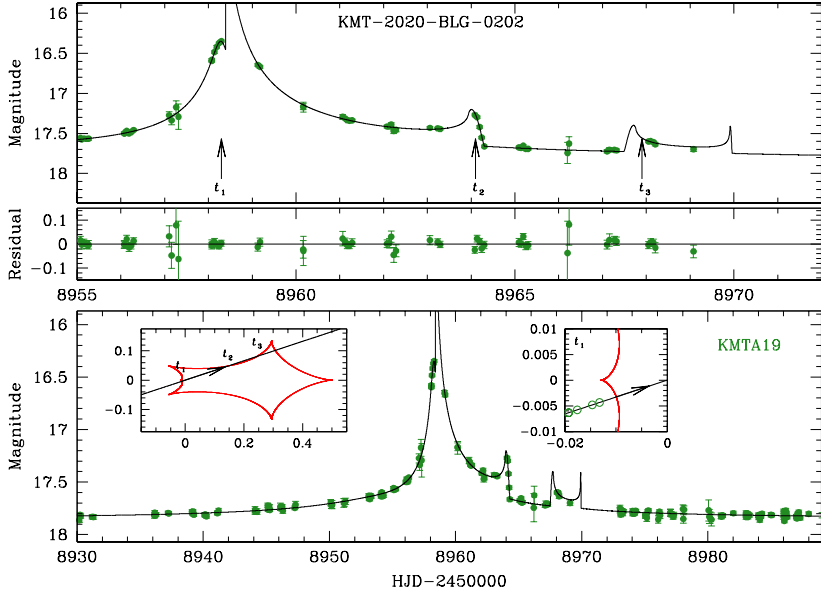


Figure 1. Light curve of the microlensing event KMT-2020-BLG-0202. The bottom panel presents the overall light curve, while the two upper panels show the zoomed-in view of the anomaly region and the residuals from the best-fit model (solid curve). The arrows labeled t_1 , t_2 , and t_3 in the top panel mark the times of the major anomalies. The left inset in the bottom panel illustrates the lens-system geometry, depicting the source trajectory (arrowed line) with respect to the caustic structure (red cuspy curve) generated by the binary lens. The source locations at the epochs of the major anomalies are indicated by labels matching those in the top panel. The right inset provides a magnified view of the configuration in the vicinity of t_1 . The small green circles along the source trajectory mark the source positions at the epochs of data acquisition. Their sizes are scaled to the actual source size.

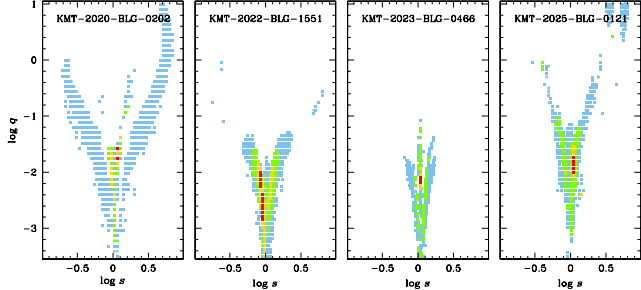


Figure 2. $\Delta\chi^2$ maps in the (s, q) grid-parameter space. The color scale indicates regions with $\Delta\chi^2 \leq n \times 1^2$ (red), $n \times 2^2$ (yellow), $n \times 3^2$ (green), and $n \times 4^2$ (cyan), where $n = 10$ for KMT-2020-BLG-0202 and KMT-2022-BLG-1551, $n = 4$ for KMT-2023-BLG-0466, and $n = 15$ for KMT-2025-BLG-0121.

heliocentric Julian date $\text{HJD}' \equiv \text{HJD} - 2450000 = 8956$. The baseline magnitude of the source is $I_{\text{base}} = 17.84$. During most of the 2020 season, two KMTNet telescopes, KMTC and KMTS, were shut down due to the COVID-19 pandemic. Consequently, the event was observed solely by the KMTA telescope, which remained operational throughout the 2020 season.

Figure 1 shows the lensing light curve of the event. Despite the relatively sparse coverage due to single-telescope observations, the light curve exhibits an ex-

tended complex anomaly pattern comprising three major features around $t_1 = 8958.3$, $t_2 = 8964.1$, and $t_3 = 8967.9$. From the sharp rises and falls, it is likely that these features result from caustic crossings of the source star. Based on the pattern, the two features at t_1 and t_2 appear to form a pair corresponding to the source's caustic entrance and exit. The feature at t_3 also appears to result from a caustic entrance, although the corresponding exit was not covered. The anomalous region constitutes an important portion of the light curve, and it was therefore initially suspected that the anomaly was produced by a binary lens composed of two components with roughly equal masses.

Despite the significant deviation from the typical short-duration anomaly pattern, the anomaly was determined to be of planetary origin. Modeling of the light curve yielded a unique solution with binary parameters of $(s, q) \sim (1.16, 14.4 \times 10^{-3})$. The left panel of Figure 2 presents the corresponding $\Delta\chi^2$ map in the (s, q) plane. We note that similarly unique solutions are obtained not only for KMT-2020-BLG-0202 but also for the other events, as shown in the remaining maps. The complete set of lensing parameters for the event is presented in Table 3, and the model light curve is shown as a solid line in Figure 1. The mass ratio is approximately 15 times greater than that between Jupiter and the Sun. Con-

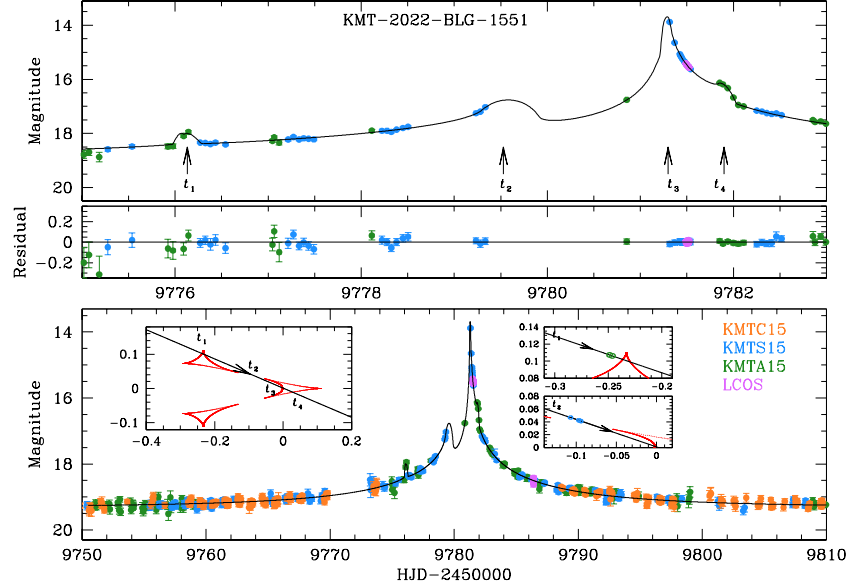


Figure 3. Lensing light curve of KMT-2022-BLG-1551. Notations are consistent with those used in Fig. 1. The two right insets in the bottom panel show zoomed-in views of the lens-system configurations around t_1 and t_2 , respectively. The small circles along the source trajectory mark the source positions near the time of the anomaly, with their sizes scaled to the source radius and their colors matching those in the legend.

Table 3. Lensing parameters of KMT-2020-BLG-0202 and KMT-2022-BLG-1551.

Parameter	KMT-2020-BLG-0202	KMT-2022-BLG-1551
χ^2	427.0	1858.9
t_0 (HJD')	8958.779 ± 0.031	9781.3238 ± 0.0027
u_0 (10^{-3})	0.031 ± 0.621	0.71 ± 0.29
t_E (days)	34.50 ± 1.50	19.31 ± 0.65
s	1.1577 ± 0.0059	0.8840 ± 0.0027
q (10^{-3})	14.39 ± 1.79	5.26 ± 0.57
α (rad)	2.822 ± 0.016	3.581 ± 0.022
ρ (10^{-3})	0.736 ± 0.068	3.13 ± 0.29

NOTE— HJD' \equiv HJD – 2450000.

sidering that Galactic microlensing events are typically produced by low-mass stellar hosts (C. Han & A. Gould 2003), the companion mass is likely below the upper planetary limit of $\sim 13 M_J$. The event timescale is estimated to be $t_E \sim 35$ days. From the resolved caustic feature around t_2 , the normalized source radius was measured to be $\rho \sim 0.74 \times 10^{-3}$.

The configuration of the lens system is shown in the inset of the bottom panel of Figure 1. The caustic induced by the binary lens forms a single resonant structure comprised of six folds meeting at six cusps. The source traversed the caustic from the lower-left to the upper-right. It initially passed near the left on-axis cusp

and subsequently crossed the lower-left fold. These interactions generated a complex light-curve morphology, including a weak bump at $HJD' \sim 8958.3$ and a sharp caustic spike at $HJD' \sim 8958.6$. Owing to the concavity of the caustic fold, the source reentered the caustic by passing through a different portion of the upper fold and finally exited through the upper-right fold. The first caustic passage of the source corresponds to the t_1-t_2 caustic pair, while the second passage corresponds to another caustic pair with the entrance at t_3 . The light-curve pattern between t_1 and t_2 deviates from a typical U-shaped profile because the source approached the upper fold asymptotically while moving inside the caustic.

3.2. KMT-2022-BLG-1551

The lensing event KMT-2022-BLG-1551 occurred on a source with a baseline magnitude of $I_{\text{base}} = 19.48$ during the 2022 season. It was detected by the KMTNet survey on 2022 July 19 (HJD' = 9779), approximately two days before the event reached a very high magnification of $A_{\text{max}} \sim 425$. Because the peak region of a high-magnification event is highly sensitive to planetary perturbations (K. Griest & N. Safizadeh 1998), follow-up observations were conducted with the LCOS telescope shortly after the peak. In addition, KMTS activated its “auto-followup” mode, in which the cadence was increased to about 3.5/hr, beginning at approximately $HJD' \sim 9781.42$ and continuing until the end of the night at ~ 9781.54 .

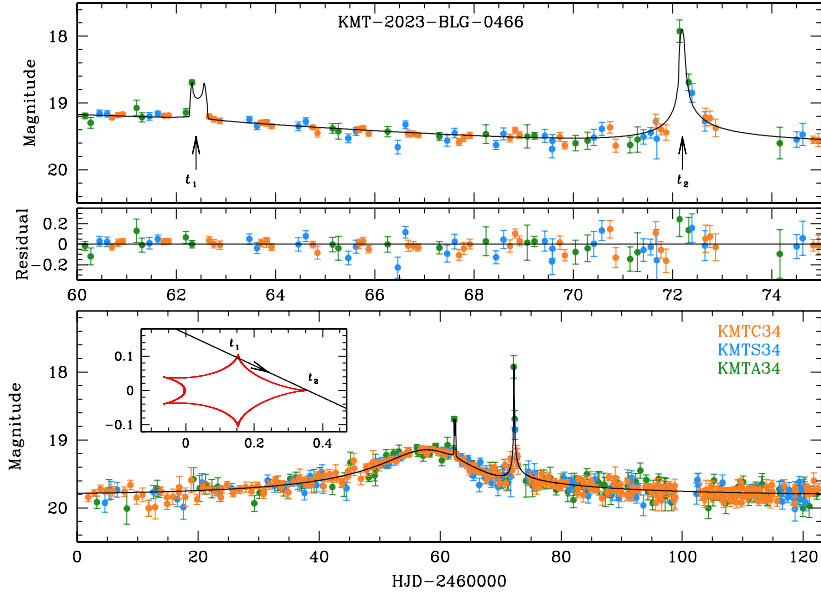


Figure 4. Light curve of the lensing event KMT-2023-BLG-0466. The notation is the same as in Figure 1.

Figure 3 shows the lensing light curve of KMT-2022-BLG-1551. The peak region exhibits an extended and complex anomaly pattern composed of multiple distinct features. The first brief anomaly feature appears at $t_1 \sim 9776.1$, followed by a smoother feature at $t_2 \sim 9779.5$. The third and fourth features, forming a caustic pair, occur at $t_3 \sim 9781.3$ and $t_4 \sim 9781.9$, respectively. No KMT-C data were obtained during the anomaly because the telescope was under maintenance. The anomaly region spans nearly one-third of the total event timescale, deviating from the typical morphology of a planetary perturbation.

Despite the atypical anomaly pattern, modeling of the light curve indicates that the perturbations were produced by a planetary companion to the primary lens. The unique binary-lens solution yields parameters $(s, q) \sim (0.88, 5.3 \times 10^{-3})$ and an event timescale of $t_E \sim 19$ days. Analysis of the anomaly features affected by finite-source effects provides a normalized source radius of $\rho \sim 3.1 \times 10^{-3}$. Table 3 lists the complete set of lensing parameters for the event, and Figure 3 presents the model light curve.

The inset in the bottom panel of Figure 3 shows the configuration of the lens system. The planet induces two sets of caustics: a central caustic consisting of four folds, and two planetary caustics, each composed of three folds located above and below the planet–host axis. The source trajectory passes through both the central and planetary caustics. It first crossed the tip of the upper planetary caustic and then moved through the region between the central and planetary caustics, producing the successive anomaly features at t_1 and t_2 . Subse-

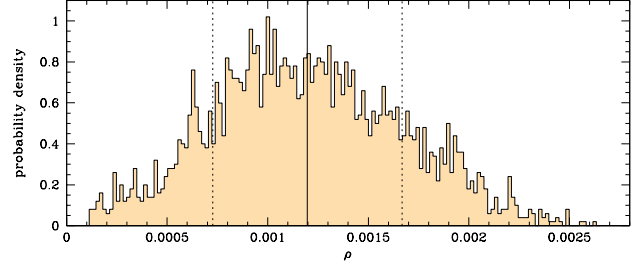


Figure 5. Distribution of the normalized source radius in the MCMC chain for KMT-2023-BLG-0466. The vertical solid line denotes the mean value, and the two dotted lines mark the 1σ interval.

quently, the source traversed the central caustic, giving rise to the pair of caustic-crossing features observed at t_3 and t_4 .

3.3. KMT-2023-BLG-0466

The lensing-induced flux magnification of the event KMT-2023-BLG-0466 was first detected on 2023 April 18 ($HJD' \equiv HJD - 2460000 = 52$), before the light curve reached a moderate peak magnification of $A_{\max} \sim 6.5$. After the peak, the light curve exhibited multiple anomalies.

Figure 4 shows the lensing light curve of the event. The first anomaly occurred at $HJD' \sim 62.4$ (t_1) and the second at $HJD' \sim 72.2$ (t_2). Although each feature appears to be a short-term perturbation of a typical planetary signal, their successive occurrence with a time interval of 9.8 days makes the overall anomaly unusual. While the second anomaly was covered by multiple data points from all three KMTNet telescopes, the first was

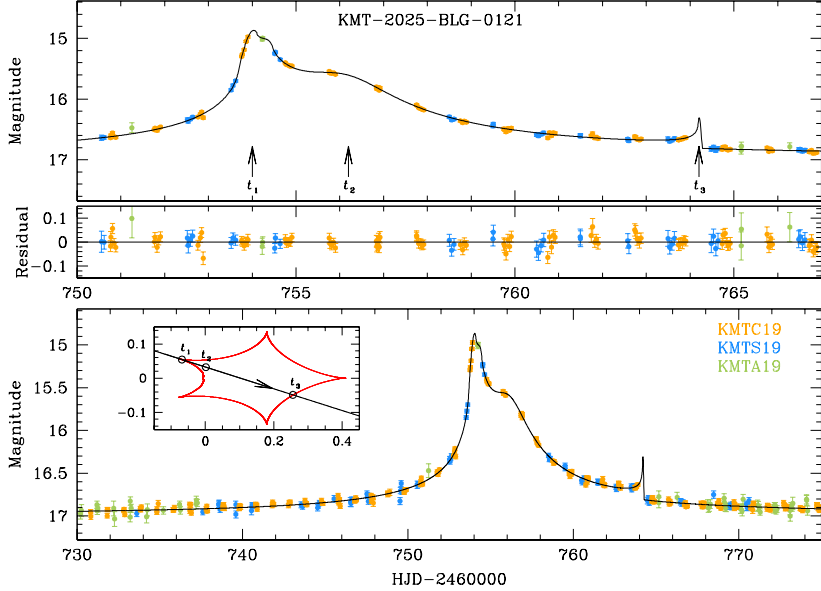


Figure 6. Light curve of the lensing event KMT-2025-BLG-0121.

recorded by a single data point from KMTA. At first glance, the KMTA data point at t_1 appeared to be an outlier, but subsequent modeling confirmed that it is a genuine signal. Owing to its large temporal separation from the feature at t_2 , it tightly constrains the source trajectory and, consequently, the remaining lensing parameters.

The 2L1S modeling yielded a unique solution with binary parameters of $(s, q) \sim (1.08, 7.0 \times 10^{-3})$. The low mass ratio indicates that the companion to the lens is a planetary object. The event timescale is $t_E \sim 43$ days. To assess whether the normalized source radius is actually constrained, we examined its distribution in the MCMC chain. As shown in Figure 5, the distribution indicates that ρ is measured, although its uncertainty remains substantial because the anomaly is only partially covered. Table 4 lists the complete set of lensing parameters for the solution, and Figure 4 shows the corresponding model light curve.

The inset in the bottom panel of Figure 4 shows the lens-system configuration of the event. The planetary lens produces a resonant caustic similar in shape to that of KMT-2020-BLG-0202. However, the source trajectory relative to the caustic is markedly different. Rather than crossing the caustic, the source passes along its outer region, grazing it twice—first near the upper cusp and then near the right on-axis cusp. These two grazing encounters produce the anomaly features observed at t_1 and t_2 . Because of the large size of the caustic and the spatial separation between the two source-caustic encounters, the resulting anomalies appear well separated in time.

Table 4. Lensing parameters of KMT-2023-BLG-0466 and KMT-2025-BLG-0121.

Parameter	KMT-2023-BLG-0466	KMT-2025-BLG-0121
χ^2	998.8	1880.2
t_0 (HJD')	58.15 ± 0.14	756.463 ± 0.020
u_0 (10^{-3})	0.1505 ± 0.0082	0.0311 ± 0.0010
t_E (days)	43.43 ± 1.68	29.97 ± 0.54
s	1.0779 ± 0.0037	1.0912 ± 0.0026
q (10^{-3})	6.97 ± 0.89	12.1 ± 0.74
α (rad)	3.577 ± 0.012	3.449 ± 0.011
ρ (10^{-3})	1.20 ± 0.47	1.13 ± 0.08

NOTE—HJD' \equiv HJD – 2460000.

3.4. KMT-2025-BLG-0121

The lensing event KMT-2025-BLG-0121 occurred on an apparently bright source with a baseline magnitude of $I_{\text{base}} = 16.97$. The event was detected during its early magnification phase on 2025 March 18 (HJD' = 752).

The light curve of the event is presented in Figure 6. It exhibits a noticeable asymmetry with respect to the peak at HJD' = 754.0 (t_1). The portion of the light curve following t_1 displays two distinct features: a smooth bump centered at HJD' = 756.2 (t_2) and a sharp caustic spike at HJD' = 764.2 (t_3). Together, these features form an extended anomaly that occupies a substantial fraction of the light curve, making it difficult to infer its planetary origin based solely on the observed light-curve morphology.

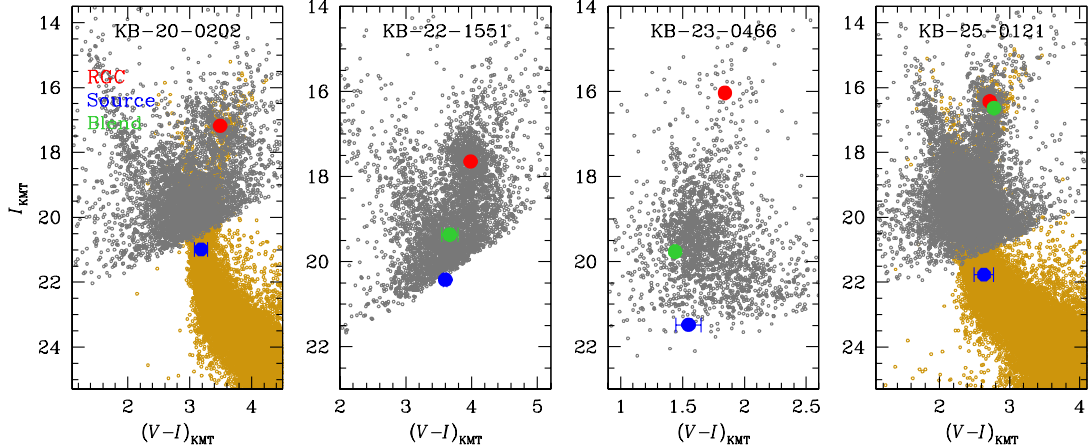


Figure 7. Locations of the source and the centroid of the red giant clump (RGC) in the instrumental color-magnitude diagrams (CMDs). For the two events KMT-2020-BLG-0202 and KMT-2025-BLG-0121, the source colors were estimated using combined CMDs constructed from KMT observations (gray dots) and HST data (brown dots). For KMT-2022-BLG-1551, KMT-2023-BLG-0466, and KMT-2025-BLG-0121, the positions of the blend stars are also indicated.

Contrary to initial expectations, modeling of the light curve indicates that the anomaly was produced by a very low-mass companion to the primary lens. The light curve is uniquely described by a solution with binary parameters $(s, q) \sim (1.09, 12.1 \times 10^{-3})$ and an event timescale of $t_E \sim 30$ days. Table 4 lists the complete set of lensing parameters, and the model light curve is shown as a solid line in Figure 6. The event is found to be heavily blended, indicating that the relatively bright baseline flux is dominated by blended light rather than by the source itself. The normalized source radius was precisely determined from the well solved anomaly feature around t_1 .

The configuration of the lens system is illustrated in the inset of the lower panel of Figure 6. The planetary lens produces a resonant caustic structure similar in morphology to those of KMT-2020-BLG-0202 and KMT-2023-BLG-0466. The source traverses the caustic diagonally, entering through the upper-left cusp and exiting through the lower-right fold. The peak at t_1 corresponds to the time when the source entered the caustic, while the bump around t_2 arises as the source asymptotically approached a nearby caustic fold. The feature at t_3 corresponds to the time of the caustic exit.

4. ANGULAR EINSTEIN RADIUS

For a lensing event with a measured normalized source radius, the angular Einstein radius can be determined as

$$\theta_E = \frac{\theta_*}{\rho}, \quad (2)$$

where θ_* denotes the angular radius of the source. Measuring the angular Einstein radius is crucial for constraining the physical lens parameters because it is re-

lated to the lens mass (M) and distance (D_L) as

$$\theta_E = \sqrt{\kappa M \pi_{\text{rel}}}. \quad (3)$$

Here $\kappa = 4G/(c^2 \text{AU})$ and $\pi_{\text{rel}} = \text{AU}(D_L^{-1} - D_S^{-1})$ is the relative lens-source parallax, and D_S denotes the distance to the source. For all analyzed events, the normalized source radii were measured. Therefore, to determine θ_E , it is necessary to estimate θ_* .

We estimated the angular radius of the source star from its reddening- and extinction-corrected (de-reddened) color and magnitude, $(V - I, I)_0$. The procedure was as follows. First, we measured the instrumental magnitudes of the source in the V and I bands. Second, we located the source on the color-magnitude diagram (CMD) constructed from stars in the vicinity of the event. Third, we calibrated the source's color and magnitude using a reference feature in the CMD whose de-reddened values are known. Finally, we derived the angular radius of the source from an empirical relation between stellar color, magnitude, and angular radius.

We measured the source magnitude by fitting the observed light curve with the model. For this purpose, we used light curves processed with the pyDIA photometry code (M. Albrow 2017), which was also used consistently to construct the CMD. For color and magnitude calibration, we adopted the centroid of the red giant clump (RGC) in the CMD as a reference, whose de-reddened color and magnitude were taken from previous studies by T. Bensby et al. (2013) and D. M. Nataf et al. (2013), respectively. We then derived the angular source radius using the $(V - K, I) - \theta_*$ relation. Because this relation requires the $V - K$ color, we converted the measured

Table 5. Source parameters, angular Einstein radius, and relative lens-source proper motion.

Parameter	KMT-2020-BLG-0202	KMT-2022-BLG-1551	KMT-2023-BLG-0466	KMT-2025-BLG-0121
$(V - I)$	3.184 ± 0.106	3.599 ± 0.028	1.549 ± 0.104	2.634 ± 0.139
I	20.985 ± 0.038	20.424 ± 0.001	21.484 ± 0.024	21.772 ± 0.010
$(V - I, I)_{\text{RGC}}$	$(3.492, 17.179)$	$(3.983, 17.646)$	$(1.843, 16.034)$	$(2.718, 16.430)$
$(V - I, I)_{\text{RGC},0}$	$(1.060, 14.326)$	$(1.060, 14.339)$	$(1.060, 14.538)$	$(1.060, 14.389)$
$(V - I)_0$	0.752 ± 0.106	0.675 ± 0.049	0.766 ± 0.111	0.976 ± 0.139
I_0	18.133 ± 0.038	17.117 ± 0.020	19.988 ± 0.031	19.731 ± 0.010
Spectral type	G8V	G1V (turnoff)	G7V	K2.5V
θ_* (mas)	0.780 ± 0.099	1.139 ± 0.097	0.337 ± 0.044	0.499 ± 0.078
θ_{E} (mas)	1.060 ± 0.166	0.364 ± 0.046	0.281 ± 0.116	0.442 ± 0.076
μ (mas/yr)	11.22 ± 1.83	6.89 ± 0.8	2.36 ± 0.98	5.39 ± 0.93

$V - I$ color into $V - K$ using the color–color relation of [M. S. Bessell & J. M. Brett \(1988\)](#).

For the two events KMT-2020-BLG-0202 and KMT-2025-BLG-0121, it was difficult to obtain a reliable source color because of the challenges in measuring the V -band magnitude. In these cases, we derived the source color by first aligning the CMD constructed from KMTC observations with that from HST data ([J. A. Holtzman et al. 1988](#)). We then inferred the source color as the mean value of stars along the main-sequence branch within the range corresponding to the I -band magnitude offset from the RGC centroid.

Figure 7 shows the locations of the source stars in the instrumental CMDs relative to the RGC centroid for each event. For three events—KMT-2022-BLG-1551, KMT-2023-BLG-0466, and KMT-2025-BLG-0121—the positions of the blend stars are also indicated. Table 5 summarizes the source parameters, including the instrumental color and magnitude of the source, $(V - I, I)$, and of the RGC centroid, $(V - I, I)_{\text{RGC}}$, as well as their de-reddened values, $(V - I, I)_0$ and $(V - I, I)_{\text{RGC},0}$. The table also lists the inferred spectral type and angular radius of each source. The sources are found to be main-sequence stars ranging from spectral types G to K, with angular radii between 0.34 and $1.14 \mu\text{as}$. Also presented in the table are the angular Einstein radius and relative lens-source proper motion. The relative lens-source proper motion is calculated by combining the angular Einstein radius and the event timescale according to the relation $\mu = \theta_{\text{E}}/t_{\text{E}}$.

5. PHYSICAL LENS PARAMETERS

We estimated the mass and distance of the lens system by conducting a Bayesian analysis based on the measured observables of each event. This analysis combines the measured microlensing observables t_{E} and θ_{E} with

prior information on the Galactic distribution and kinematics of potential lens and source populations. In this framework, the posterior probability distribution of the physical parameters is expressed as

$$P(M, D_{\text{L}} \mid t_{\text{E}}, \theta_{\text{E}}) \propto P(t_{\text{E}}, \theta_{\text{E}} \mid M, D_{\text{L}})P(M, D_{\text{L}}), \quad (4)$$

where the likelihood, $P(t_{\text{E}}, \theta_{\text{E}} \mid M, D_{\text{L}})$, quantifies how well a model with given M and D_{L} reproduces the observed t_{E} and θ_{E} , and the prior, $P(M, D_{\text{L}})$, represents the expected distributions of lenses and sources in the Galaxy.

The priors were derived from a Galactic model that includes the density and velocity distributions of disk and bulge stars, as well as a mass function for the lens population. In the analysis, we adopted the Galactic model of [Y. K. Jung et al. \(2021\)](#) and employed the lens mass function proposed by [Y. K. Jung et al. \(2022\)](#). Using these priors, a large number of lens-source pairs were generated via Monte Carlo simulation. For each simulated event, the observables t_{E} and θ_{E} were computed, and the likelihood of each event was evaluated as

$$L \propto \exp\left(-\frac{\chi^2}{2}\right), \quad \chi^2 = \frac{(t_{\text{E}} - t_{\text{E,obs}})^2}{\sigma_{t_{\text{E}}}^2} + \frac{(\theta_{\text{E}} - \theta_{\text{E,obs}})^2}{\sigma_{\theta_{\text{E}}}^2}. \quad (5)$$

Here, $(t_{\text{E,obs}}, \theta_{\text{E,obs}})$ denote the observed values of the lensing observables, and $(\sigma_{t_{\text{E}}}, \sigma_{\theta_{\text{E}}})$ represent their measurement uncertainties.

The posterior probability distributions of the events are shown in Figure 8 for the lens mass and in Figure 9 for the lens distance. The derived physical parameters of the lens system are summarized in Table 6, where M_{p} and M_{h} denote the masses of the planet and its host, respectively, and a_{\perp} represents the projected separation between them. The median of each posterior distribution was adopted as the representative value, and the

Table 6. Physical lens parameters.

Parameter	KMT-2020-BLG-0202	KMT-2022-BLG-1551	KMT-2023-BLG-0466	KMT-2025-BLG-0121
$M_h (M_\odot)$	$0.81^{+0.49}_{-0.36}$	$0.54^{+0.31}_{-0.28}$	$0.44^{+0.36}_{-0.27}$	$0.61^{+0.32}_{-0.32}$
$M_p (M_J)$	$12.28^{+7.37}_{-5.43}$	$2.96^{+1.71}_{-1.53}$	$3.25^{+2.59}_{-2.03}$	$7.77^{+4.08}_{-4.04}$
D_L (kpc)	$3.84^{+1.19}_{-1.18}$	$6.90^{+0.92}_{-1.33}$	$6.80^{+1.14}_{-1.60}$	$6.20^{+0.93}_{-1.35}$
a_\perp (AU)	$4.17^{+1.29}_{-1.28}$	$2.29^{+0.30}_{-0.44}$	$2.68^{+0.45}_{-0.63}$	$3.05^{+0.46}_{-0.66}$
p_{disk}	91%	34%	31%	43%
p_{bulge}	9%	66%	69%	57%

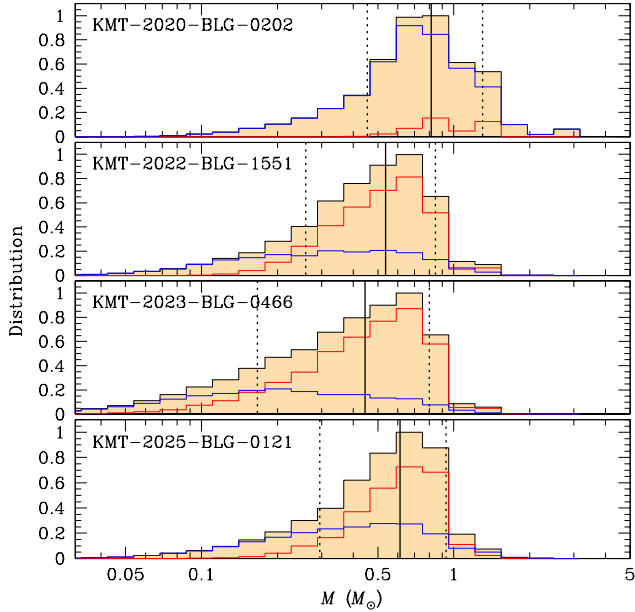


Figure 8. Posterior probability distributions of the lens mass. In each panel, the probability contributions from the disk and bulge lens populations are shown by blue and red curves, respectively, while the total distribution is indicated by a black curve. The solid vertical line represents the median of the distribution, while the two dotted vertical lines indicate the 1σ range.

lower and upper uncertainties correspond to the 16th and 84th percentiles, respectively. Also listed are the probabilities that the lens resides in the Galactic disk (p_{disk}) or in the bulge (p_{bulge}).

It is found that the companions to the lenses are super-Jupiters, with masses exceeding that of Jupiter but below the deuterium-burning threshold of $\sim 13 M_J$ (A. Burrows et al. 1997; D. S. Spiegel et al. 2011). For KMT-2020-BLG-0202L, the upper limit of the companion mass exceeds this threshold, although the median value lies below it, implying that the object may be a brown dwarf. In all cases, the host stars have masses lower than that of the Sun.

The location of the snow line is expected to scale with the host mass as $a_{\text{sl}} \sim 2.7 \text{ AU} (M/M_\odot)$

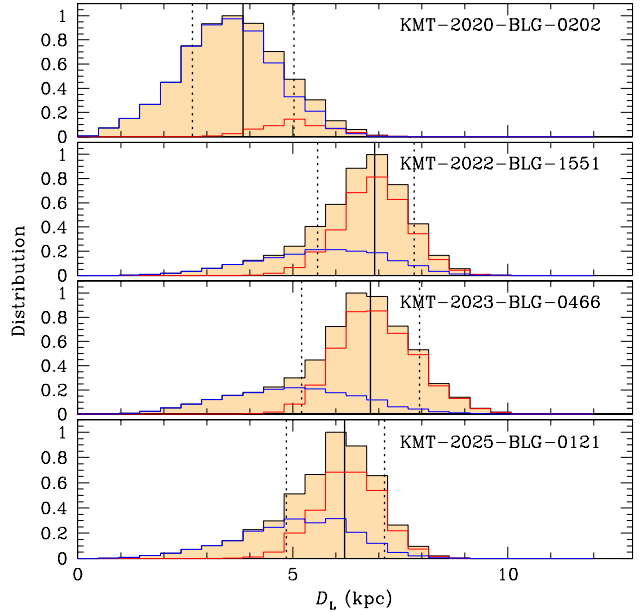


Figure 9. Posterior probability distributions of the distance to the lens.

(G. M. Kennedy & S. J. Kenyon 2008). Given that the measured a_\perp values represent projected separations, all of the detected planets lie well beyond the snow line of their respective hosts. Detection of such cold giant planets by other methods, such as the radial-velocity or transit techniques, is inherently challenging owing to their long orbital periods and the low geometric probability of transit alignment. The detections reported here therefore highlight the unique capability of the microlensing method to probe the population of cold, massive planets beyond the snow line.

The inferred lens locations differ from event to event. For KMT-2020-BLG-0202, the lens is most likely in the Galactic disk, with a probability of $p_{\text{disk}} = 91\%$. By contrast, for KMT-2022-BLG-1551 and KMT-2023-BLG-0466, the lenses are about twice as likely to reside in the bulge as in the disk. For KMT-2025-BLG-0121, the probabilities of disk and bulge membership are approximately equal.

6. SUMMARY AND CONCLUSION

We have analyzed four microlensing events—KMT-2020-BLG-0202, KMT-2022-BLG-1551, KMT-2023-BLG-0466, and KMT-2025-BLG-0121—that exhibit extended and complex anomalies in their light curves. These events were identified through a systematic reanalysis of KMTNet data aimed at recovering planetary signals that deviate from the typical short-term anomaly morphology. Detailed light-curve modeling shows that the anomalies in all four cases are produced by planetary companions orbiting low-mass stellar hosts.

The planetary systems have mass ratios in the range $q \sim (5\text{--}14) \times 10^{-3}$ and Einstein timescales of $t_E \sim 20\text{--}45$ days. Bayesian analyses based on Galactic models indicate that the companions are super-Jupiters, with masses of a few to $\sim 10 M_J$, orbiting sub-solar-mass host stars. All planets lie well beyond the snow line of their respective hosts, placing them firmly in the cold-giant regime. This population provides valuable insight into the occurrence of massive planets at wide separations, a region of parameter space largely inaccessible to other detection techniques.

These results demonstrate that extended and complex anomaly patterns—often missed by automated detection algorithms—can contain planetary signals. Failure to recover such planets would bias demographic inferences, leading to underestimated occurrence rates and distortions in the inferred planet-to-host mass-ratio function, particularly for high- q planets. Systematic reanalysis of microlensing survey data is therefore essential for constructing a more complete and less biased census of exoplanets in the Galaxy. While no approach can guarantee complete recovery of all planetary signals, sustained efforts along these lines will reduce selection biases in demographic studies and thereby improve our understanding of the formation and distribution of cold giant planets.

W. Zang et al. (2025) reported the mass-ratio distribution of planets based on KMTNet detections from the 2016–2019 seasons. Their statistical sample includes all planets detected in 2018 and 2019, whereas for earlier seasons only planets with mass ratios of order 10^{-4} and below were included because the detection efficiency for

higher- q planets had not yet been fully quantified. Consequently, of the three planets presented in Paper I, only the 2019-season event (OGLE-2019-BLG-0299Lb) is included in their analysis, while the two 2017-season events (KMT-2017-BLG-2509Lb and OGLE-2017-BLG-1099Lb) are not. The KMTNet collaboration plans to revisit this analysis with an expanded sample that incorporates planets reported since the 2020 season, including those presented here and those omitted from the initial study.

A further consideration for detection efficiency, and hence inferred demographics, is binary-lens degeneracy, although the four planets reported here are not affected by this issue given their well-constrained solutions. Y. Shang et al. (2025) showed that 2L1S degeneracies reduce survey sensitivity by $\sim 5\%\text{--}10\%$, with the impact increasing toward higher mass ratios. If neglected, this leads to underestimated planet occurrence rates and a flatter inferred mass-ratio function. Future demographic analyses should therefore incorporate degeneracy-aware sensitivity estimates to mitigate such systematic biases as microlensing samples continue to grow.

ACKNOWLEDGMENTS

C.H. was supported by the National Research Foundation of Korea (NRF) grant funded by the Korea government (MSIT: RS-2025-21073000). This research was supported by the Korea Astronomy and Space Science Institute under the R&D program (Project No. 2025-1-830-05) supervised by the Ministry of Science and ICT. This research has made use of the KMTNet system operated by the Korea Astronomy and Space Science Institute (KASI) at three host sites of CTIO in Chile, SAAO in South Africa, and SSO in Australia. Data transfer from the host site to KASI was supported by the Korea Research Environment Open NETwork (KREONET). H.Y. and W.Z. acknowledge support by the National Natural Science Foundation of China (Grant No. 12133005). H.Y. acknowledge support by the China Postdoctoral Science Foundation (No. 2024M762938).

REFERENCES

Alard, C.; Lupton, R. H. 1998, ApJ, 503, 325,
doi: [10.1086/305984](https://doi.org/10.1086/305984)

Albrow, M. 2017, MichaelDAlbrow/pyDIA: Initial Release
on Github, Version v1.0.0, Zenodo,
doi: [10.5281/zenodo.268049](https://doi.org/10.5281/zenodo.268049)

Albrow, M. D., Horne, K., Bramich, D. M., et al. 2009,
MNRAS, 397, 2009,
doi: [10.1111/j.1365-2966.2009.15098.x](https://doi.org/10.1111/j.1365-2966.2009.15098.x)

Bensby, T., Yee, J. C., Feltzing, S., et al. 2013, A&A, 549,
A247, doi: [10.1051/0004-6361/201220678](https://doi.org/10.1051/0004-6361/201220678)

Bessell, M. S., & Brett, J. M. 1988, PASP, 100, 1134, doi: [10.1086/132281](https://doi.org/10.1086/132281)

Burrows, A., Marley, M., Hubbard, W. B., et al. 1997, ApJ, 491, 856, doi: [10.1086/305002](https://doi.org/10.1086/305002)

Dong, S., DePoy, D. L., Gaudi, B. S., et al. 2006, ApJ, 642, 842, doi: [10.1086/501224](https://doi.org/10.1086/501224)

Gould, A., & Loeb, A. 1992, ApJ, 396, 104, doi: [10.1086/171700](https://doi.org/10.1086/171700)

Griest, K., & Safizadeh, N. 1998, ApJ, 500, 37, doi: [10.1086/305729](https://doi.org/10.1086/305729)

Han, C., & Gould, A. 2003, ApJ, 592, 172, doi: [10.1086/375706](https://doi.org/10.1086/375706)

Han, C., Udalski, A., Kim, D., et al. 2021, A&A, 655, A21, doi: [10.1051/0004-6361/202141517](https://doi.org/10.1051/0004-6361/202141517)

Holtzman, J. A., Watson, A. M., Baum, W. A., et al. 1988, AJ, 115, 1946, doi: [10.1086/300336](https://doi.org/10.1086/300336)

Jung, Y. K., Han, C., Udalski, A., et al. 2021, AJ, 161, 293, doi: [10.3847/1538-3881/abf8bd](https://doi.org/10.3847/1538-3881/abf8bd)

Jung, Y. K., Zang, W., Han, C., et al. 2022, AJ, 164, 262, doi: [10.3847/1538-3881/ac9c5c](https://doi.org/10.3847/1538-3881/ac9c5c)

Kennedy, G. M., & Kenyon, S. J. 2008, ApJ, 673, 502, doi: [10.1086/524130](https://doi.org/10.1086/524130)

Kim, S.-L., Lee, C.-U. and Park, B.-G., Kim, D.-J., et al. 2016, JKAS, 49, 37, doi: [10.5303/JKAS.2016.49.1.37](https://doi.org/10.5303/JKAS.2016.49.1.37)

Mao, S., & Paczyński, B. 1991, ApJL, 374, L37, doi: [10.1086/186066](https://doi.org/10.1086/186066)

Nataf, D. M., Gould, A., Fouqué, P., et al. 2013, ApJ, 769, 88, doi: [10.1088/0004-637X/769/2/88](https://doi.org/10.1088/0004-637X/769/2/88)

Shang, Y., Yang, H., Zhang, J., et al. 2025, AJ, 170, 339, doi: [10.3847/1538-3881/ae14f3](https://doi.org/10.3847/1538-3881/ae14f3)

Spiegel, D. S., Burrows, A., & Milsom, J. A. 2011, ApJ, 727, 57, doi: [10.1088/0004-637X/727/1/57](https://doi.org/10.1088/0004-637X/727/1/57)

Tomaney, A. B., & Crotts, A. P. S. 1996, AJ, 112, 2872, doi: [10.1086/118228](https://doi.org/10.1086/118228)

Wozniak, P. R. 2000, Acta Astronomica, 50, 421, doi: [10.48550/arXiv.astro-ph/0012143](https://doi.org/10.48550/arXiv.astro-ph/0012143)

Yang, H., Yee, J. C., Hwang, K.-H., et al. 2025, MNRAS, 528, 11, doi: [10.1093/mnras/stad3672](https://doi.org/10.1093/mnras/stad3672)

Yee, J. C., Shvartzvald, Y., Gal-Yam, A., et al. 2012, ApJ, 755, 102, doi: [10.1088/0004-637X/755/2/102](https://doi.org/10.1088/0004-637X/755/2/102)

Zang, W., Jung, Y. K., Yee, J. C., et al. 2025, Science, 388, 400, doi: [10.1126/science.adn6088](https://doi.org/10.1126/science.adn6088)